Materials and Design 189 (2020) 108481

Contents lists available at ScienceDirect

Materials and Design

journal homepage: www.elsevier.com/locate/matdes

Revealing relationships between porosity, microstructure and mechanical properties of laser powder bed fusion 316L stainless steel through heat treatment

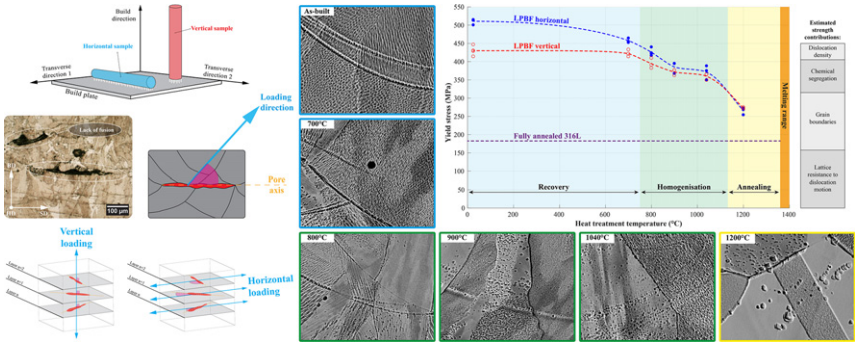
Tobias Ronneberg, Catrin M. Davies, Paul A. Hooper*

Department of Mechanical Engineering, Imperial College London, SW7 2AZ, UK

HIGHLIGHTS

- Laser powder bed fusion 316L samples are heat treated and characterised.
- Microstructural features are related to anisotropic yield behaviour.
- Anisotropic ductility is related to the shape, size and orientation of porosity.
- Heat treatments are categorised by recovery, homogenisation and annealing regimes.

GRAPHICAL ABSTRACT



ARTICLE INFO

Article history:
Received 9 October 2019
Received in revised form 29 November 2019
Accepted 6 January 2020
Available online 18 January 2020

Keywords:
Additive manufacturing
Laser powder bed fusion
316L stainless steel
Characterisation
Yield behaviour
Failure behaviour

ABSTRACT

The understanding of relationships between processing, microstructure and mechanical properties in laser powder bed fusion is currently incomplete. Microstructure-property relations in 316L stainless steel are revealed in this study using isothermal heat treatments as an investigative tool. As-built material was heat treated to selectively remove microstructural features such as melt pool boundaries, microsegregations and the as-built grain structure to evaluate their influence on yield and failure behaviour. Anisotropic yield behaviour was found to be caused by microstructural features alone and not influenced by porosity. However, ductility and failure were dominated by lack of fusion porosity. The alignment of pores between tracks along layer boundaries was found to cause anisotropic ductility. Three strengthening mechanisms in as-built material were identified as grain boundaries, chemical segregation and dislocation density. Heat treatments were categorised into three regimes: recovery, homogenisation and annealing. The findings of this study show that the shape, size, orientation and distribution of pores are crucial parameters for evaluating the structural integrity of parts produced by laser powder bed fusion.

© 2020 The Authors. Published by Elsevier Ltd. This is an open access article under the CC BY license (http://creativecommons.org/licenses/by/4.0/).

1. Introduction

Laser powder bed fusion (LPBF) produces unique microstructures which can compete favourably with other manufacturing processes [1]. However, LPBF cannot simply replace more conventional manufacturing methods because the materials produced have distinct properties and many microstructure-property relationships remain unclear [2-4]. The microstructure is influenced by various process parameters, allowing for microstructure manipulation by parameter adjustments. Understanding the effects of microstructural features on material properties is therefore vital to produce parts with optimised microstructures and superior properties.

* Corresponding author.
E-mail address: paul.hooper@imperial.ac.uk (P.A. Hooper).

https://doi.org/10.1016/j.matdes.2020.108481
0264-1275/© 2020 The Authors. Published by Elsevier Ltd. This is an open access article under the CC BY license (http://creativecommons.org/licenses/by/4.0/).

In the case of 316L stainless steel, LPBF manufactured material in the as-built state is often significantly stronger than traditionally manufactured material and may also achieve high ductility [5-7]. LPBF material is generally anisotropic with both strength and ductility approximately 10% greater in the build plane (horizontal) than the build direction (vertical) in the as-built state [8,9]. These properties are often attributed to microstructural features, but the individual contribution of each type of feature remains unclear [10-13].

The microstructure of as-built LPBF 316L is complex due to the intensity and speed of the heat source which induces large thermal gradients and non-equilibrium solidification structures [14-16]. It is characterised by overlapping melt pools and columnar grains aligned with the build direction and containing fine subgranular cellular structures [17-22]. Electron backscatter diffraction (EBSD) analyses have found grains to be around 10–500 μm long, and each grain contains a substructure of parallel cells approximately 500 nm wide that reveal the grain's solidification direction by their orientation [10,12,23-26]. Cell walls contain higher concentrations of chromium and molybdenum than the cells' interiors, as well as higher dislocation densities [7,17,18]. The misorientation between cells in a grain is very small ($<1^\circ$), but between different grains the misorientation can be any angle [10,11,27]. Grain boundaries and cell walls inhibit dislocation movement and thus strengthen the material [17].

Traces of scan tracks are revealed by bands of segregated solutes known as melt pool boundaries [26]. These reflect the borders of adjacent scan tracks within the same layer (track-track) and between layers (layer-layer) [12,28]. Grains often protrude through layer boundaries indicating epitaxial grain growth, particularly when the local thermal gradient aligns with a preferred growth direction in the solid crystal [11,24]. Melt pool boundaries are suspected of being weak regions of the material as failure along melt pool boundaries has been observed [21,26].

The largest phase by volume apart from austenite in LPBF 316L is gas inside pores [15,28-30]. Although porosity is generally undesirable and considered a material defect rather than a feature, it will nonetheless remain important for LPBF part qualification in the foreseeable future. Porosity is generated by a variety of mechanisms including lack of fusion, keyhole-mode melting and gas absorption [14,20,22,31,32]. No authoritative standard exists to qualify LPBF materials, but there is growing consensus that at least 99.5% of theoretical density is required to qualify as 'highly dense' [33-36]. Relative density can be determined by a number of methods including the Archimedes method, image analysis of polished sections and X-ray computed tomography techniques [37,38].

The aim of this work is to clarify the relationships between porosity, microstructure and mechanical properties in LPBF 316L. Porosity was characterised by image analysis of large sections to determine the distribution of shape, size and orientation of pores and relative density of samples. The influence of microstructural features was investigated by subjecting samples to heat treatments designed to gradually dissolve these features. Through metallography and tensile testing of samples built in different orientations, the relative contribution of different features could be assessed. Sections of tensile samples tested to failure were analysed to evaluate the effects of microstructural features and porosity on failure behaviour.

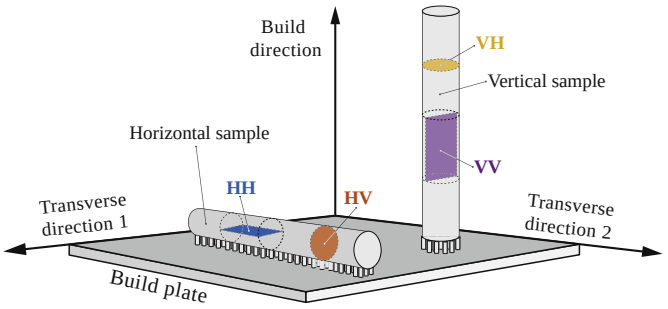


Fig. 1. Orientations of cylindrical samples and sections for metallographic examination relative to the build direction.

2. Materials and experimental methods

2.1. Sample production and heat treatment

Test samples for this study were produced in a commercial Renishaw AM250 LPBF machine using manufacturer-recommended process parameters. 316L powder was supplied by LPW Technology Ltd. which consisted of 15–45 μm spherical particles of the nominal composition given in Table 1. Cylinders 70 mm long by 10 mm diameter were built with their axis in vertical (along the build direction) and horizontal (normal to the build direction) orientations on 5 mm supports in argon atmosphere (see Fig. 1). The pulsing 200 W laser was focused to a 65 μm spot. Points on the powder bed separated by 60 μm were exposed for 80 μs, giving the process an approximate scanning speed of 750 mm/s. The hatch spacing and layer thickness were 110 μm and 50 μm respectively. The 'chessboard' scanning strategy was used with 67° rotation of the scanning direction between layers for most samples while a small set was produced using the 'meander' strategy with no rotation between layers [39]. Upon completion of the build, the cylinders were removed from the build plate by cutting through the support structures.

Samples were subjected to varying levels of heat treatment ranging from no post-processing (the 'as-built' condition) to an annealing treatment expected to fully recrystallise the microstructure. These isothermal heat treatments were conducted in a Nabertherm N 41/H chamber furnace [40]. Samples were placed in the preheated furnace filled with air and held for 60 min before being moved to ambient conditions and allowed to cool in air to room temperature. The holding temperatures were 700 °C, 800 °C, 900 °C, 1040 °C and 1200 °C, the latter representing full annealing. These temperatures were set and measured using the furnace temperature controller.

2.2. Metallography and porosity analysis

As-built and heat treated samples were sectioned to examine horizontal and vertical surfaces in both build orientations as illustrated in Fig. 1. The four surfaces are labelled 'HH', 'HV', 'VH' and 'VV', where the first letter indicates the build orientation of the sample and the second letter is the section plane orientation. Sectioned samples were mounted in epoxy castings and ground flat with SiC

Table 1
Powder nominal chemical composition. Single values designate maximum concentrations.

Element	C	Si	P	S	Cr	Mn	Fe	Ni	Cu	Mo
wt%	0.03	0.75	0.025	0.01	17.5–18.0	2.0	Balance	12.5–13.0	0.5	2.25–2.50

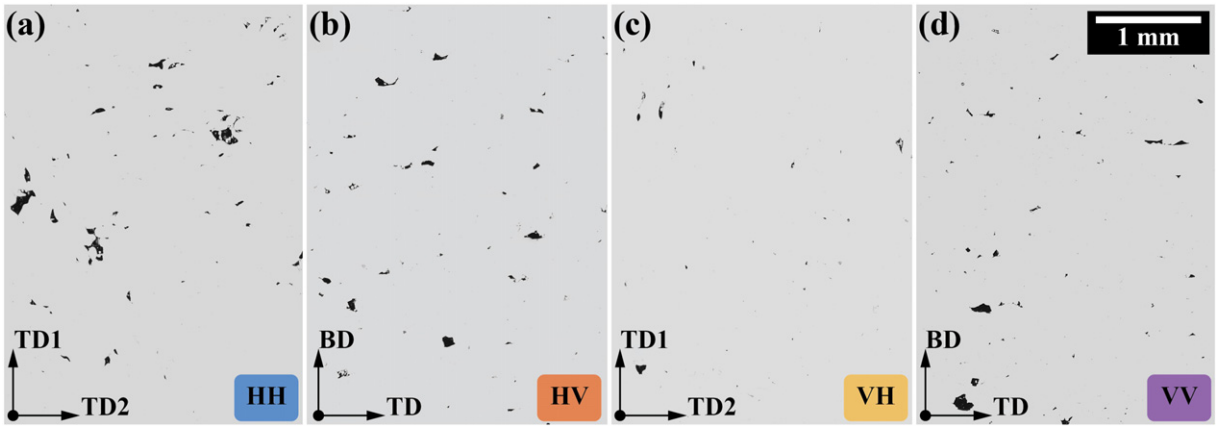


Fig. 2. Optical micrographs of polished sections showing porosity in (a) horizontal sample horizontal section, (b) horizontal sample vertical section, (c) vertical sample horizontal section and (d) vertical sample vertical section. Black areas identify porosity in the section. BD designates the build direction while TD designates transverse directions (i.e. directions in the build plane).

grinding papers. Mechanical polishing with diamond suspensions down to 1 μm was followed by final polishing using 0.06 μm colloidal silica suspension. The samples were electrolytically etched in 10% oxalic acid solution applying a potential difference of 5 V for 90 s to reveal the microstructure [41]. Etched samples were examined in a Zeiss Axioscope optical microscope and a Hitachi S-3400N scanning electron microscope (SEM). Applying an accelerating voltage of 13 kV at around 8 mm working distance produced a good signal for the backscattered electron (BSE) detector in the SEM.

Material porosity was characterised by image analysis of polished surfaces. Samples were imaged and digitally stitched together to extend the field of view using a Hirox RH-2000 digital microscope at a resolution of 2.61 μm/pixel. A total area of at least 1000 mm^2 was imaged of each section shown in Fig. 1 to attain a statistically significant sample size of pores to be analysed. The composite images were analysed in ImageJ software. Area, fit ellipse and Feret's diameter parameters were recorded for each pore using the 'Analyse Particles' function [42]. Objects smaller than 25 μm^2 (<4 pixels) were filtered out to exclude sample preparation artefacts from the data. The distribution of size, shape and orientation of pores and area fraction porosity was calculated in each orientation. The representative size of each pore was estimated by the mean of Feret's diameter, maximum fit ellipse length and root of area. Volumetric relative density was estimated by the geometric mean of area fraction porosity in horizontal (f_H) and vertical (f_V) sections of each sample using Eq. (1). The geometric mean is more conservative than the arithmetic as it gives greater weight to the section with more porosity.

$$\text{Relative density} = \sqrt{(1-f_H)\times(1-f_V)} \quad (1)$$

2.3. Tensile testing and post-test examination

Cylinders in as-built and heat treated conditions were machined into circular tensile specimens of 20 mm gauge length and 4.0 mm diameter in accordance with tolerances described in ASTM standard E8/E8 M [43]. Samples were speckled using spray paint prior to testing so strain could be measured by digital image correlation (DIC) using the point-to-point method (virtual extensometer). Tensile testing to failure was conducted quasistatically at a strain rate not exceeding $5 \cdot 10^{-4}$ s^{-1}. The gauge surface was photographed every 2 s using a 200 mm macro lens attached to a DSLR camera. The images were processed in GOM Correlate DIC software to calculate nominal engineering strain [44]. Tests were repeated at least twice for each condition (orientation and heat treatment).

A post-test examination of fractured tensile samples was conducted by cold mounting and grinding samples with SiC papers to section the fracture surface longitudinally. These samples were polished and etched to reveal the microstructure near the fracture surface. The deformed subsurface microstructure was imaged using the Hirox RH-2000 digital microscope and Zeiss Axioscope optical microscope.

3. Results and discussion

3.1. Image analysis and porosity characterisation

Fig. 2 shows representative areas of polished samples used for porosity analysis. The larger pores in all samples were irregularly shaped and some contained powder particles, meaning they can be characterised as lack of fusion pores [45-47]. Table 2 presents key results from the image analyses to characterise porosity in each build orientation. Note that the total area analysed for each section is much larger than the representative sections shown in Fig. 2 (see total area column in Table 2). A large cross-sectional area was required to produce adequate statistics to characterise porosity.

The pores were sorted by size into 10 μm intervals to produce the size distribution plots presented in Fig. 3. The top row shows histograms of pore size frequency while the plots below show the area fraction of all the pores in each interval relative to the total area of the section. All the relative frequency plots in the top row show

Table 2
Key results of the image analysis of polished samples in different orientations.

Sample build orientation	Section name	Total area (mm^2)	Area fraction porosity (%)	Relative density (%)	Average aspect ratio	Average angle to build plane (°)
Horizontal	HH	1140	0.66	99.39	2.5	–
	HV	1099	0.55		2.6	31
Vertical	VH	1113	0.26	99.59	3.1	–
	VV	1232	0.54		2.4	30

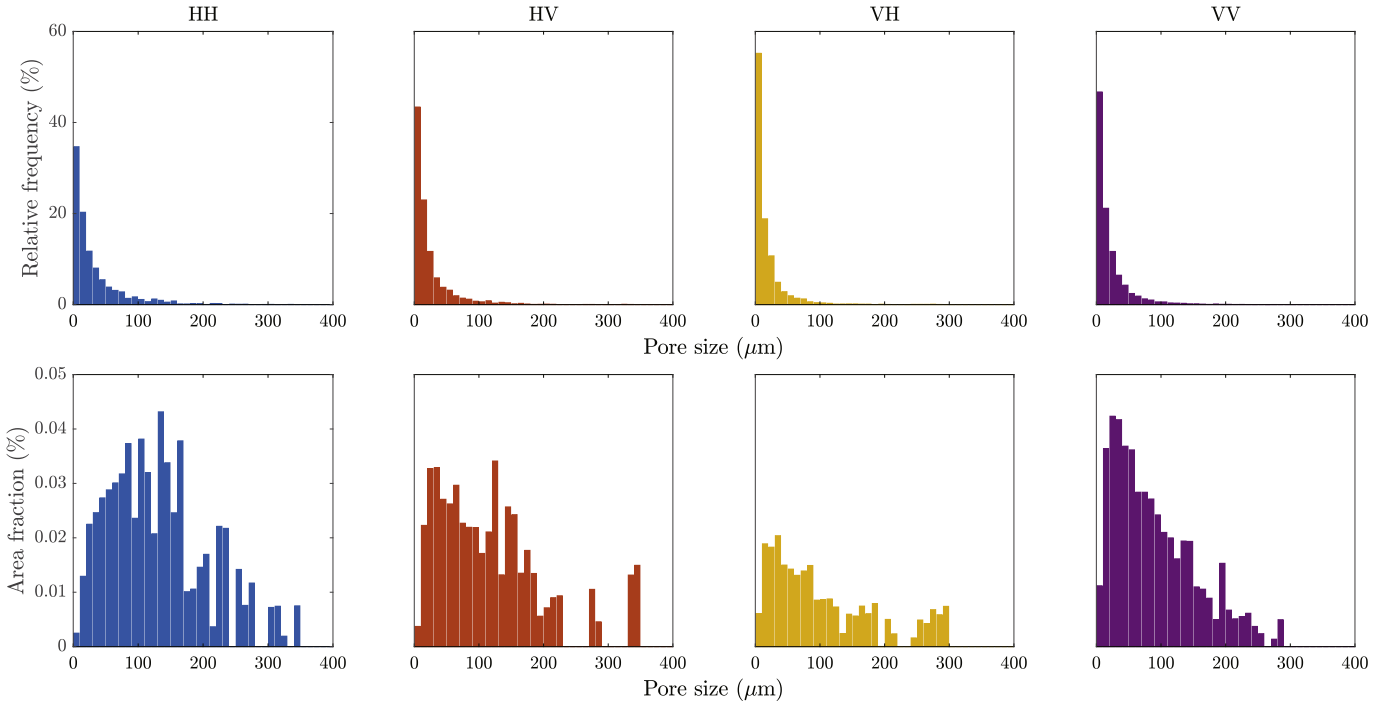


Fig. 3. Pore size distribution histograms showing relative frequency of pores (top) and fraction of the total area (bottom) in different sections.

exponential decay from a peak near zero so the smallest pores are most abundant and scarcity increases with pore size in all sections. However, the relative area fraction plots below show much of the porosity is contained in a few larger pores. No pores larger than 400 μm were found in any of the sections, but the distributions confirm that large pores are found in all sections as was shown in Fig. 2. All the bottom plots also contain a single peak, but these peaks are shifted to size values substantially greater than zero. The lack of multiple peaks makes it difficult to distinguish between types of porosity (such as keyhole mode and lack of fusion pores) by size alone.

In Fig. 4, the pore size is plotted against the cumulative area fraction of pores in each section. To account for pores too small to be analysed (<5 μm), linear regression of pores smaller than 30 μm was used to calculate the required offsets for the curves to tend to zero. All four sections have similarly shaped curves in the figure. The cumulative area fraction porosity rises rapidly with pore size at first, but later converges toward a horizontal asymptote. The total area fraction porosity in each section is labelled in the figure, and this value is clearly near the associated asymptote. The horizontal sample's horizontal section (HH) was the most porous and Fig. 4 shows this is due to a relative abundance of larger pores. The least porous section was the vertical sample's horizontal section (VH), which was found to have relatively few pores of all sizes. The variation in porosity between sections can be caused by a number of factors. The laser window lens, gas filter and powder recoater blade all degrade with time during the LPBF process [48]. Such degradation will affect part quality unevenly both over the build plate and in the build direction, leading to quality variations between samples.

Pore aspect ratio is plotted against pore size in Fig. 5. For small pores (<30 μm), the data is affected by image resolution as maximum aspect ratio increases with the number of pixels describing

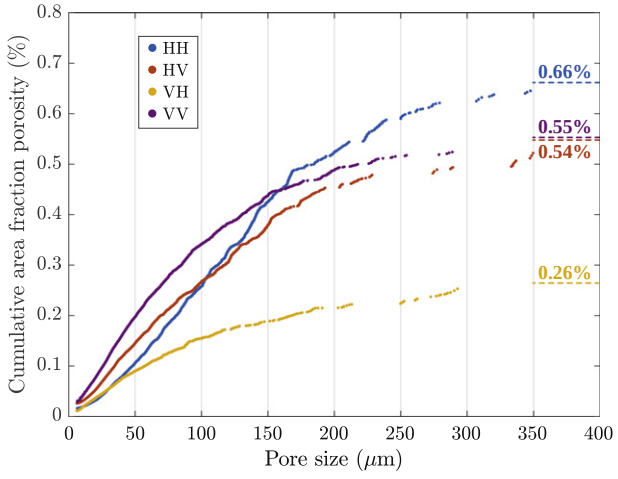


Fig. 4. Cumulative area fraction porosity vs pore size in different orientations. Dotted lines show the total amount of porosity in the section.

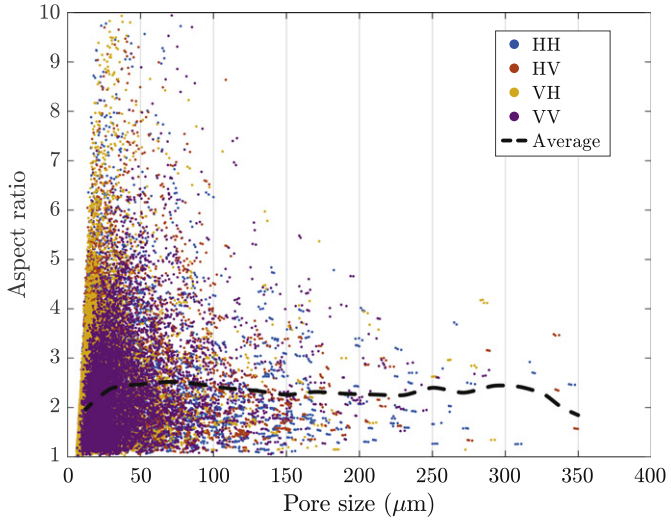


Fig. 5. Pore aspect ratio plotted against pore size in different build orientations and sections.

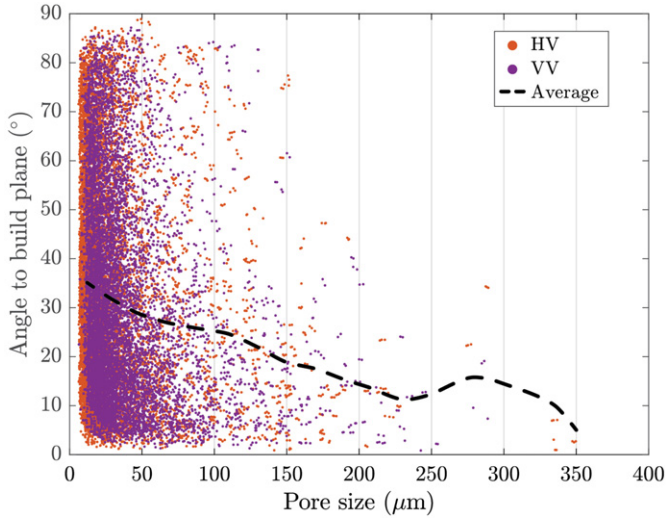


Fig. 6. Angle between the major axis and the build plane plotted against pore size for all pores in vertical samples.

the pore. For larger pores, the maximum aspect ratio decreases with increasing size. However, sorting the data into 20 μm size intervals and taking the mean value of each interval reveals a different trend as shown by the black line labelled 'Average'. The average aspect ratio is stable for all pore sizes and orientations. Thus, the apparent decrease in aspect ratio with size reflects increasing scarcity of larger pores. Average aspect ratio numbers in Table 2 are calculated from pores larger than 30 μm in the samples. However, as sectioning always occurs at an angle to the major axis of pores the aspect ratio is systematically underestimated.

The angle between the major axis of a pore and the build plane is plotted against size for all pores in vertical sections (HV and VV) in Fig. 6. Angles are in the range 0–90° where 0° represents horizontal pores aligned with the layer boundaries and 90° represents vertical pores aligned with the build direction. Grouping the data into 20 μm size intervals reveals the average angle decreases with pore size. The smallest pores (<20 μm) may appear evenly distributed in all orientations, but the grouped data indicates preference for horizontal alignment with an average angle of 34° instead of 45° as would be expected from a random distribution. The preference becomes stronger with increasing pore size. The standard deviation from the average values was 23° and 20° for HV and VV respectively, and 89% of pores larger than 100 μm were aligned within 45° of the build plane. Therefore, despite scatter in the data there is a tendency for large pores to be oriented horizontally along the layer boundaries.

3.2. Porosity and microstructure of as-built material

Fig. 7 presents the microstructure of as-built LPBF 316L material. The microstructure is consistent with LPBF microstructures characterised elsewhere in literature [17,21]. Melt pool boundaries are visible and the rotating scanning strategy is evident from the different melt pool shapes. 'Layer-layer' melt pool boundaries identify the line of fusion between layers, while 'track-track' boundaries identify the edge of overlap to an adjacent scan track [22,24,28]. Columnar grains of various sizes are generally oriented toward the build direction and frequently grow through melt pool boundaries. Grains can terminate abruptly at boundaries, but most meet other grains inside melt pools as expected from competitive growth. Each grain contains a cellular structure with low-angle boundaries as shown in the SEM micrograph in Fig. 7b. Most large pores are found on layer boundaries, particularly at junctions where a layer-layer boundary meets a track-track boundary.

Fig. 8 shows etched surfaces of LPBF 316L produced with no rotation between layers. A section normal to the scanning direction (SD) is presented in Fig. 8a which shows the microstructure consists of melt pools lying directly on top of each other. The view is rotated 90° about the build direction in Fig. 8b where the melt pools are sectioned in the scanning direction normal to the hatching direction (HD). The lack of fusion pores have different geometries in the two sections. In Fig. 8a, the pores are small with low aspect ratio and are located at junctions of track-track and layer-layer boundaries. In the side view shown in Fig. 8b, the pores are elongated along the layer-layer boundaries. Such lack of fusion pore geometry have been observed elsewhere in literature [22,31,32,45].

Various types of insufficient melt pool overlap are shown in Fig. 9. The meander scanning strategy with no rotation between layers is assumed. Fig. 9a shows the front view with the scanning direction out of the plane. A normal melt pool section is shown to the left which has good overlap with surrounding melt pools. The three melt pools to the right have abnormal shapes leading to areas with no overlap marked in red, similar to work done by Tang et al. [46]. Low energy density (ED) may produce a melt pool too small to sufficiently overlap with neighbouring melt pools. However, excessive energy density can cause evaporation in the melt pool and the classic keyhole shape. Such melt pools have deep penetration, but the shape may cause insufficient overlap with adjacent melt pools as shown in the figure. The shape on the right shows a disrupted melt pool. Instability may be caused by a number of factors including surface tension variations, spatter and inclusions. The latter represented by a green particle in the figure.

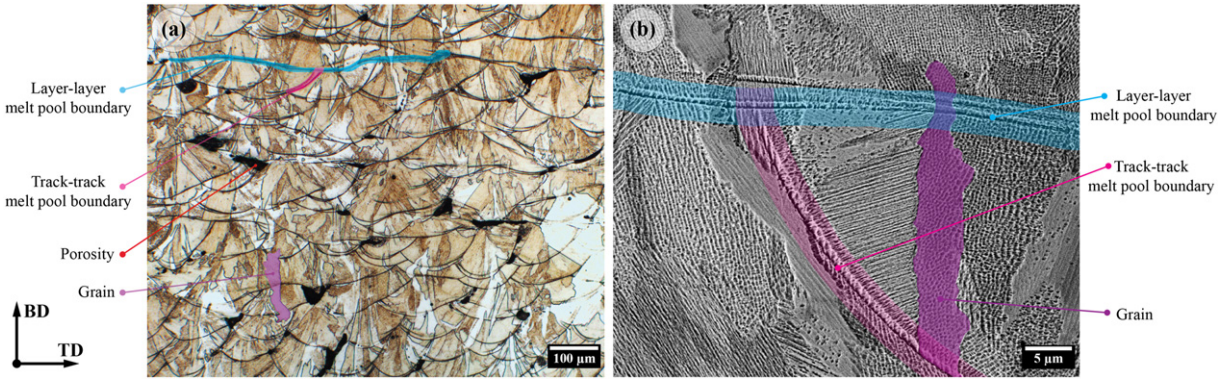


Fig. 7. Annotated as-built material microstructure images acquired by a) optical microscopy and b) SEM.

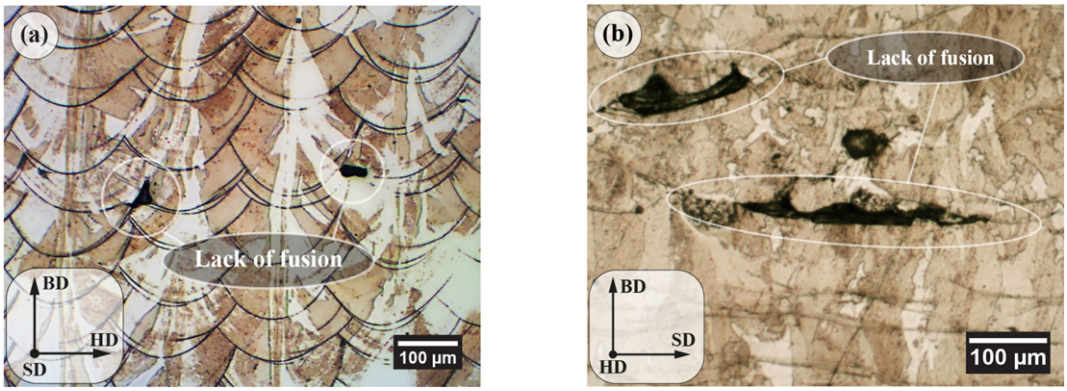


Fig. 8. Etched sections of as-built material produced with no rotation of the scanning direction between layers. (a) Front view with the scanning direction (SD) into the page. (b) Side view with the scanning direction in the page.

All the abnormal melt pool shapes in Fig. 9a form areas of insufficient overlap leading to lack of fusion. These relatively small areas have low aspect ratios in this section, but Fig. 9b shows another section rotated by 90° about the build direction. When lack of fusion is initiated at a layer-layer melt pool boundary, it may be extended during the process in the scanning direction along the layer boundary. Therefore, the lack of fusion pores have high aspect ratios and preferred alignment with layer boundaries in the scanning direction. This theory is in agreement with the images shown in Fig. 8 as well as the findings from image analysis in Section 3.1 that lack of fusion pores have clear preference with regard to orientation relative to the build direction.

3.3. Microstructural evolution with heat treatment

Figs. 10 and 11 show optical and SEM images respectively of samples heat treated at various temperatures. Looking only at the six optical micrographs in Fig. 10, it would appear the overall grain structure is not highly affected by heat treatment up to 1040 °C as it is only the 1200 °C sample that features a substantially different grain structure with much larger grains and annealing twins [49]. However, the SEM images in Fig. 11 show that microstructural changes do occur at lower temperatures on a smaller scale. There is little evidence of new grain nucleation in the sample heat treated at 1200 °C and some traces of the as-built structure remain.

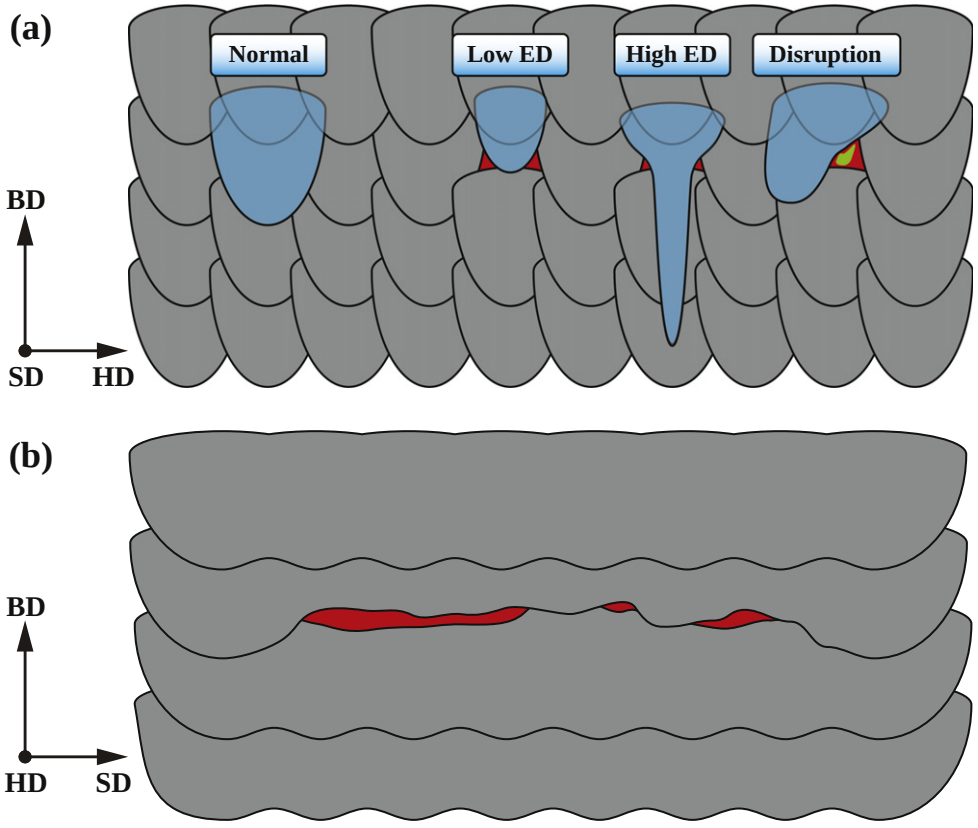


Fig. 9. Illustration of insufficient melt pool overlap leading to lack of fusion at melt pool junctions, leading to porosity and reduced bulk density. (a) Front view showing different mechanisms of inadequate overlap. (b) Side view showing how a small region of poor overlap can be extended along layer boundaries.

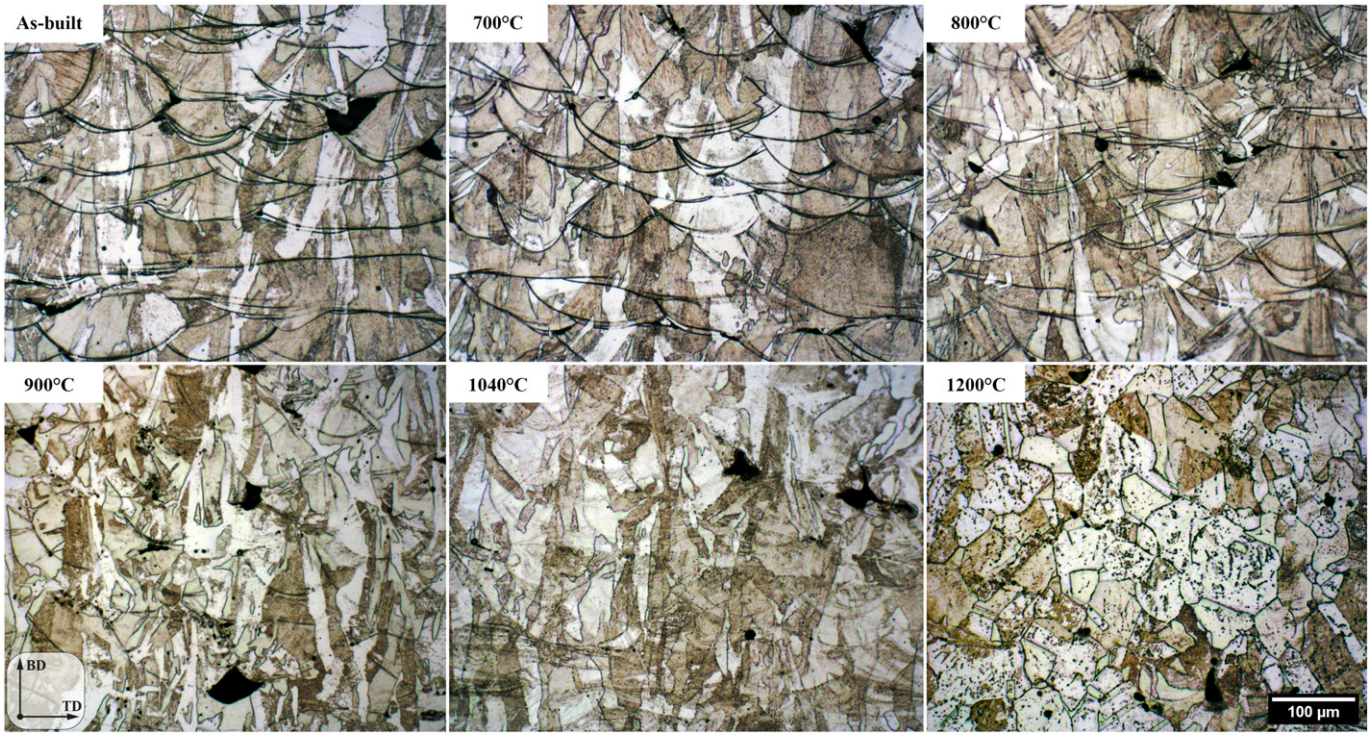


Fig. 10. Optical micrographs of etched as-built and heat treated samples.

While the microstructures presented in Figs. 10 and 11 show resilience to grain growth up to 1040 °C, the melt pool boundaries gradually disappear at lower temperatures. Such boundaries are thin bands of slightly different composition to the melt pool interior [12]. Their presence after heat treatment suggests little atomic diffusion was induced while their dissolution is evidence of significant diffusion. The melt pool boundaries appear largely unaffected by heat treatment at 700 °C, but at 800 °C they become thinner and less distinguishable from grain boundaries. The contrast between the melt pool boundary and interior is also reduced. After heat treatment at 900 °C, the melt pool boundaries have clearly started to dissolve and only vague traces are evident after heat treatment at 1040 °C. Atomic diffusion therefore gradually becomes significant over the temperature range 700–1040 °C for 60 min heat treatments. This is substantiated by the dissolution of subgranular cellular structures with increasing heat treatment temperature shown by the SEM images in Fig. 11. Cell walls consist of higher dislocation density and higher concentrations of heavy elements relative to

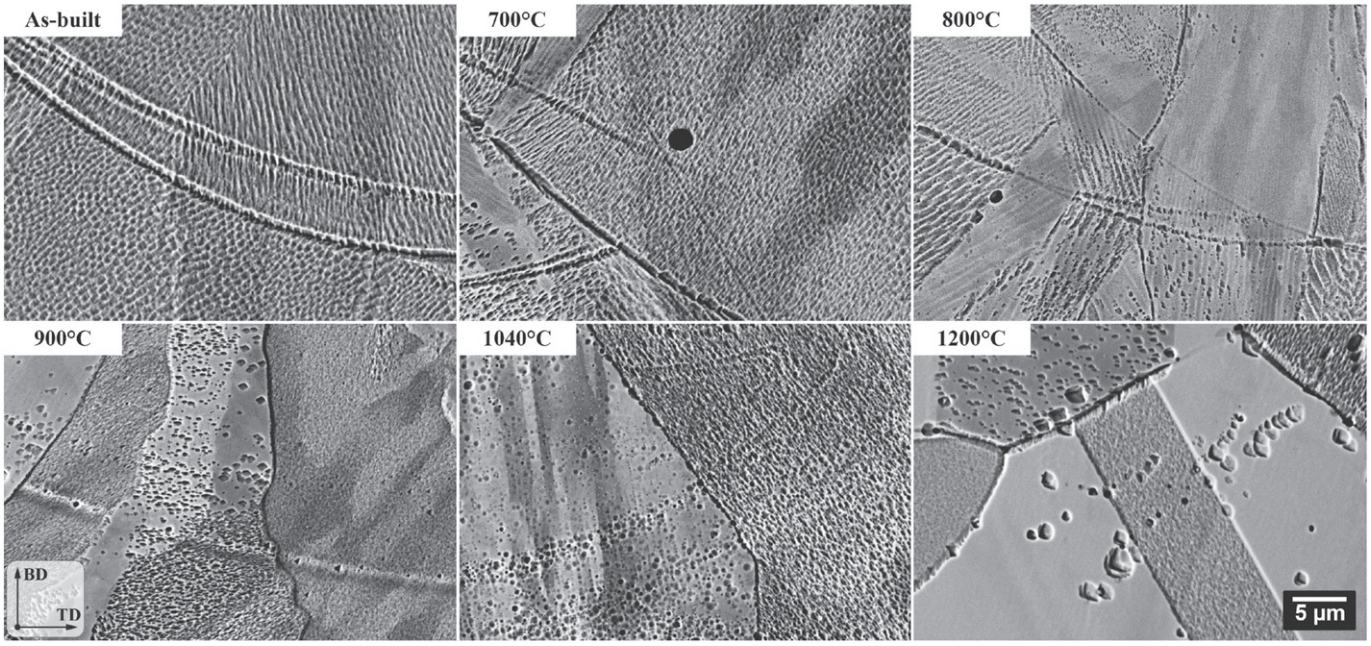
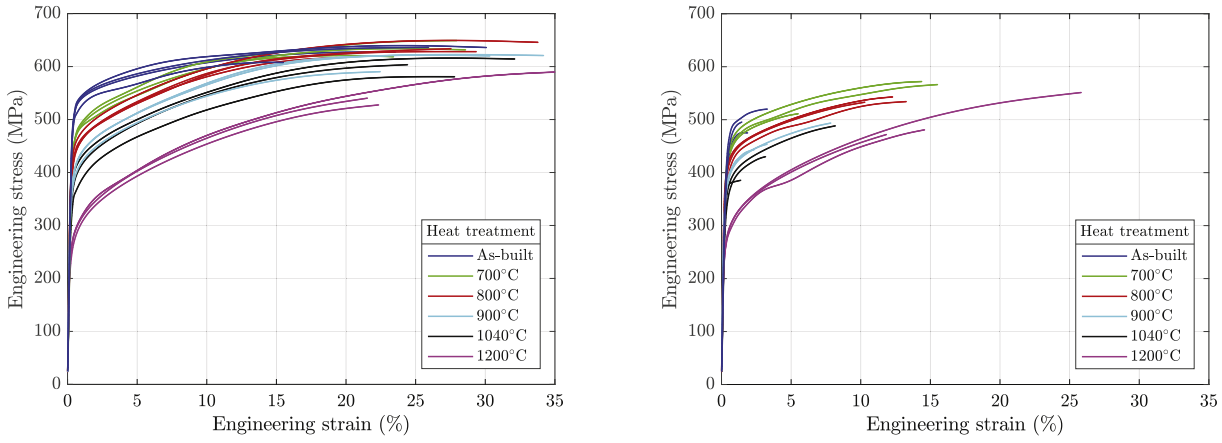


Fig. 11. SEM images of as-built and heat treated samples.



(a) Horizontally built samples

(b) Vertically built samples

Fig. 12. Engineering stress-strain curves resulting from tensile tests of cylindrical samples built in a) horizontal and b) vertical orientation. The colours indicate the isothermal heat treatment temperature prior to testing. All tensile tests were conducted at room temperature. (For interpretation of the references to colour in this figure legend, the reader is referred to the web version of this article.)

cell interiors, both of which can provide contrast in backscattered electron (BSE) SEM images [7,17,18]. Fig. 11 shows the cellular structure dissolves over a similar heat treatment temperature range as the melt pool boundaries (700–1040 °C). This is reasonable as both cell walls and melt pool boundaries are chemical segregations. When chemical segregations are dissolved by diffusion the grains become homogeneous. Controlling the heat treatment temperature and time can therefore adjust the homogeneity of the material. The samples heat treated at 1200 °C in Figs. 10 and 11 feature some evidence of pitting corrosion assumed to be caused by the specimen preparation. Otherwise, the grains have been fully homogenised by the annealing heat treatment as all traces of the cells have been dissolved.

3.4. Yield behaviour evolution vs heat treatment

The curves in Fig. 12 present data up to the onset of necking in horizontal and vertical build orientations. The elongation at break was greater for horizontal samples than vertical samples on average for all heat treatments. However, there was significant variability between samples of each condition except for as-built vertical samples which showed consistent poor ductility (0.5–3.2% elongation at break). The majority of samples present low ductility compared to values of 30–60% quoted in literature [2,8,9,13]. This low ductility is attributed to the relatively high level of porosity in the material.

Yield strength is plotted against heat treatment temperature in Fig. 13. As-built samples, represented at 25 °C in the figure, show

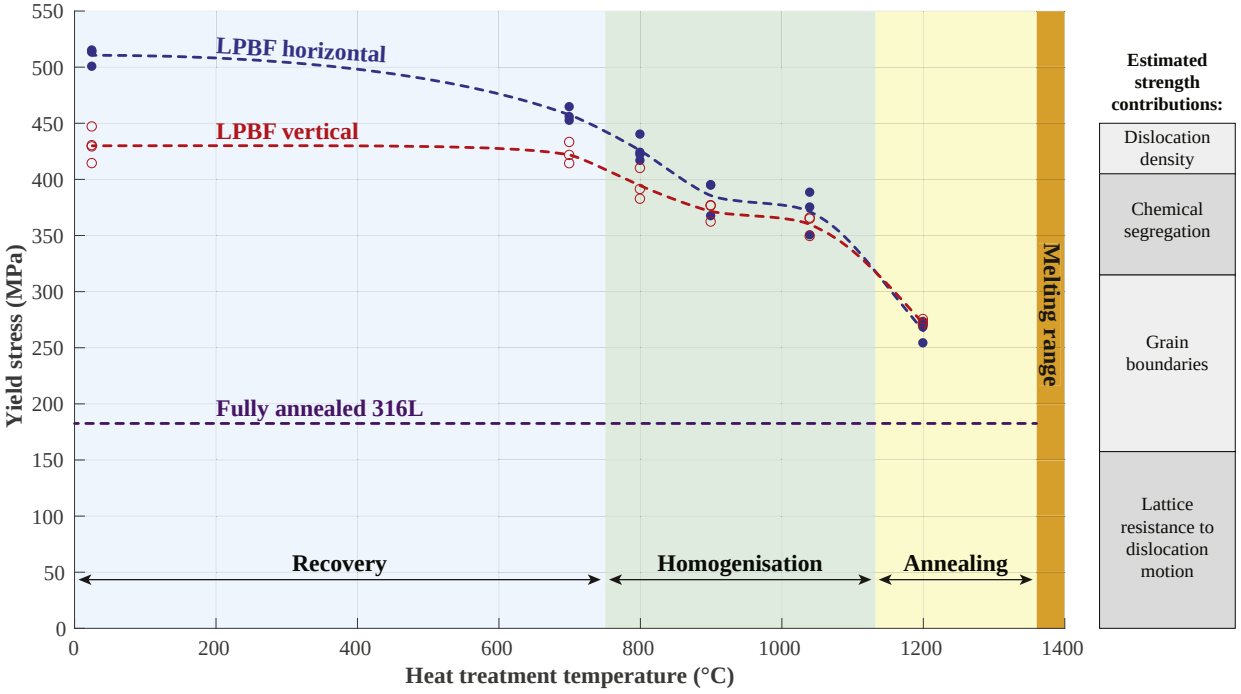


Fig. 13. Yield strength plotted against heat treatment temperature. The dotted lines represent the average yield strength for horizontal and vertical samples, along with the yield strength of a fully annealed 316L sample. As-built samples are represented at 25 °C. The coloured fields identify temperature ranges of microstructural changes observed in the metallographic analyses described in Section 3.3. (For interpretation of the references to colour in this figure legend, the reader is referred to the web version of this article.)

clear anisotropy as all horizontal samples start yielding at higher stresses than all vertical samples (19% greater on average). However, the strength of all as-built samples (in both orientations) was more than twice that reported for fully annealed 316L material (170 MPa [5]) represented by the line labelled 'Fully annealed' in Fig. 13. This line is horizontal because a fully annealed microstructure is unaffected by further heat treatment.

Figs. 12 and 13 show monotonic reduction of average yield strength with increasing heat treatment temperature in both build orientations. However, as shown by the converging curves in Fig. 13 the anisotropy diminishes with increasing heat treatment temperature. The average difference between horizontal and vertical sample yield strengths was reduced from 19% in the as-built condition to 8% after heat treatment at 700 °C. The average values for samples heat treated at 1200 °C were almost identical in both orientations, suggesting the material was transformed through heat treatment to become isotropic with regard to yield strength.

Porosity in the material was unaffected by any of the heat treatments as they were conducted at atmospheric pressure and all holding temperatures were well below the melting range of 316L. Since the yield anisotropy was eliminated by heat treatment, this means the cause must be microstructural and not related to porosity. The curves shown in Fig. 13 resemble work by Clarebrough et al. [50] relating electrical resistivity and hardness to heat treatment temperature. Differential scanning calorimetry (DSC) was used to measure the release of stored energy during annealing of deformed metals and two distinctive energy peaks were identified. A lower temperature peak was related to dislocation annihilation and a higher temperature peak was related to recrystallisation. Both peaks coincided with a reduction in electrical resistivity, and the electrical resistivity vs annealing temperature plots look very similar to the curves in Fig. 13 where two drops in yield strength are observed. The first is a small drop at lower heat treatment temperature (700–800 °C) and the second is a larger drop at higher temperature (1040–1200 °C).

Optical and SEM images in Figs. 10 and 11 show no clear microstructural changes between as-built samples and those heat treated at 700 °C, but the reduction in yield strength shown in Fig. 13 suggests some reduction in dislocation density. In conventional material processing, cold working hardens a material by increasing the dislocation density while heat treatments reducing the dislocation density are referred to as 'recovery'. Although LPBF materials are generated in a state of high dislocation density, the term 'recovery' may be useful to describe heat treatments that reduce dislocation density.

Different background colours are used in Fig. 13 to categorise heat treatments into regimes based on microstructural changes. Figs. 10 and 11 show atomic diffusion becomes significant between 700 °C and 800 °C, so heat treatments up to 750 °C are part of the 'Recovery' regime of Fig. 13. The main microstructural change of such heat treatments is a reduction in dislocation density. In the same manner, Figs. 10 and 11 show substantial grain growth first begins at a temperature between 1040 °C and 1200 °C. The temperature range from 1120 °C to the beginning of the melting range (1371 °C [8]) is therefore called as the 'Annealing' regime where significant grain growth occurs. Between recovery and annealing is the 750–1120 °C range called the 'Homogenisation'. Heat treatments in this regime induce atomic diffusion to dissolve microsegregations such as cell walls and melt pool boundaries. Note that the temperature ranges of the recovery, homogenisation and annealing regimes are not measured precisely in this investigation and will change with the holding time and cooling rate of the heat treatment.

The right side of Fig. 13 illustrates the approximate relative contributions of different microstructural features to the yield strength of as-built LPBF 316L. Fully annealed 316L has been reported to have a yield strength of 170 MPa, most of which can be attributed to lattice resistance to dislocation motion [5]. Figs. 10 and 13 show substantial grain growth and reduced in yield strength between samples heat treated at 1040 °C and 1200 °C. Grain boundaries therefore provide significant strengthening to the material. Samples near the lower end of the homogenisation regime (700 °C) were stronger than those near the upper end (1040 °C), so chemical segregations also provide considerable further strengthening. The remaining strength of as-built material is attributed to dislocation density, which was partially relieved by the recovery heat treatment at 700 °C.

All three strengthening mechanisms as well as crystal texture contribute to yield strength anisotropy. If the grain structure is textured, the average Schmidt factor will vary with the direction of loading [51]. The columnar grains are aligned with the build direction so the number of grain boundaries a dislocation has to overcome will vary with the loading direction. Likewise, cells tend to grow from melt pool boundaries upwards toward the melt pool centre. This causes cell walls (chemical segregation) to prefer alignment with the build direction making their strength contribution anisotropic as well. Finally, the dislocation density at any location in a part is affected by the thermal history of that point. The dislocation density may therefore be different in horizontal and vertical samples as heat buildup and cooling conditions will be different.

Another source of strengthening suggested in literature is nanoparticles (chromium oxides and silicates) which have been observed at cell walls [18,26,34,52]. Such particles have a hardening effect and would not be affected by heat treatment. However, their contribution has been calculated to be around 5–10 MPa, which would only account for around 2% of as-built material strength [17]. Particle hardening is therefore less significant than grain boundary strengthening, chemical segregation and dislocation density for strengthening LPBF 316L.

3.5. Ductility and failure behaviour

Elongation at break is plotted against heat treatment temperature for all samples in Fig. 14. Horizontal samples are consistently much more ductile than vertical samples, which indicates there are features in the material impervious to heat treatment that make it anisotropic with regard to ductility. In addition, and despite significant scatter in the data of both orientations, increasing trends between heat treatment temperature and ductility may be inferred as well (the positive slopes of the regression lines). This suggests

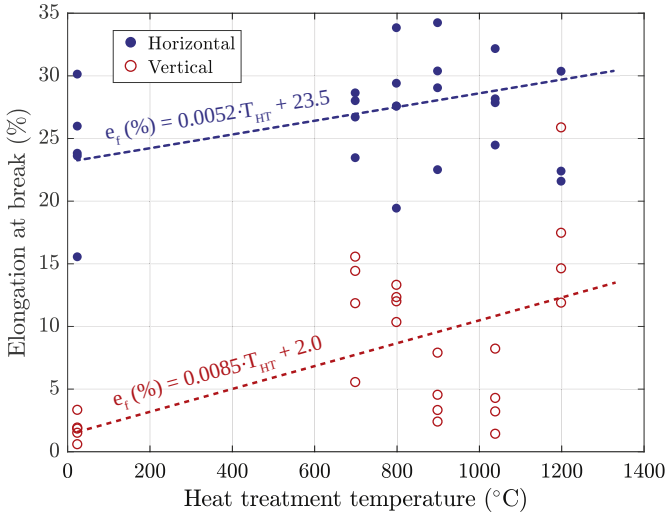


Fig. 14. Elongation at break vs heat treatment temperature of all tensile tests. Dotted lines show linear regression of average ductility values from samples tested at each heat treatment temperature.

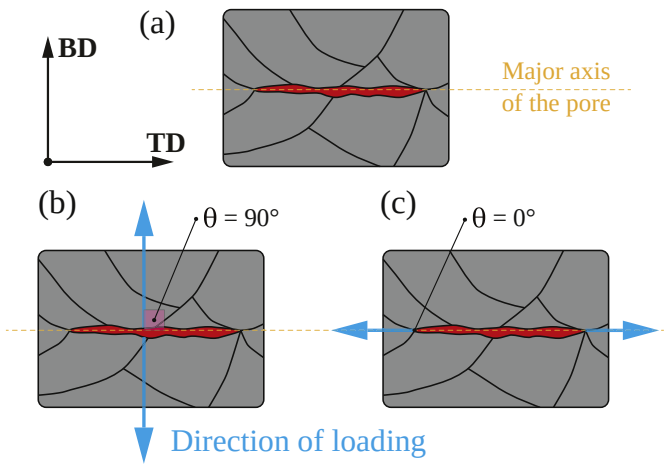


Fig. 15. Illustrations showing the angle between the direction of loading and the major axis of a lack of fusion pore at a layer boundary. a) Major axis of the pore in unloaded state. b) Loading applied normal the major axis. c) Loading applied parallel to the major axis.

microstructural changes caused by heat treatment also contribute to increasing the ductility of the material.

The most obvious cause of consistent differences in ductility is porosity. However, the analysis described in Section 3.1 found horizontal samples were more porous than vertical samples (0.61% vs 0.31% respectively). Relative density is therefore not always an accurate indicator of ductility. The analysis found pores were larger in horizontal samples and such large pores preferred alignment with layer boundaries in both horizontal and vertical samples. Fig. 15 illustrates how the angle between the direction of loading and the major axis of the pore (the longest dimension) can vary from 0° to 90°. From a structural integrity point of view, the least favourable angle is 90° as shown in Fig. 15b where stress is applied normal to the major axis of a pore. This configuration maximises the stress concentrations at the apexes of the pore to induce crack initiation or ductile void growth. Compare this to Fig. 15c where stress is applied parallel to the major axis ($\theta = 0°$). This configuration minimises stress concentrations and requires greater load to initiate void growth.

Fig. 16 shows how the angle between pore orientation (major axis) and direction of loading differs in horizontal and vertical samples built using 67° rotation about the build direction between layers. Three successive layers are shown in each sample, and every layer contains a lack of fusion pore elongated in the scanning direction along the layer boundary. For the vertical sample in Fig. 16a, the direction of loading is normal to all the pores because the load is applied normal to the layer boundaries. However, in the horizontal sample shown in Fig. 16b the angle varies from 0° to 90° between layers due to the 67° rotating scanning strategy. The angle is particularly unfavourable every 8^{th} layer when $\theta = 90 \pm 4°$ (because $67 \cdot 8 = 90 \cdot 6 - 4$).

The images in Fig. 2 show the porosity is not evenly distributed, but instead forms clusters in certain areas. This is highlighted in Fig. 17 where etched sections of as-built samples are displayed. Note in particular the inset of Fig. 17b where large pores have formed in a line. The scanning direction is rotated by 90° on either side of this line, indicating it is the edge of a square from the chessboard scanning strategy employed. Such clusters of large lack of fusion pores on a single layer may explain why some vertical samples failed at very low strains. If such a random distribution of pores over the section is representative of the material as a whole, then ductility is largely determined by whether large pores are unfavourably clustered and oriented relative to the loading direction. This explains the large variability in ductility between samples subjected to the same heat treatment, reflected in the scatter of the data in Fig. 14.

3.6. Analysis of fracture subsurface material

Fig. 18 presents an etched section of a vertical as-built sample tested to failure occurring at 1.46% elongation. The fracture surface is almost perfectly normal to the direction of loading as fracture took place within just 200 μm or four 50 μm layers. Sintered powder particles are visible across the surface, indicative of multiple lack of fusion pores within the same layer. Meanwhile, the microstructure immediately below the surface is virtually indistinguishable from unstressed as-built material, suggesting significant ductile deformation was limited to material very close to the fracture surface. The implication of these observations is that fracture occurred by coalescence of lack of fusion pores by crack growth along the layer boundaries. The inset in Fig. 18 shows the crack path was affected by the local microstructure. Much of the fracture surface follows layer-layer melt pool boundaries, while sudden shifts in the surface profile occur at junctions where melt pool boundaries meet (labelled 'boundary junction' in the figure).

The equivalent section of a horizontal as-built sample is shown in Fig. 19. This sample was more ductile failing at 25.9% elongation.

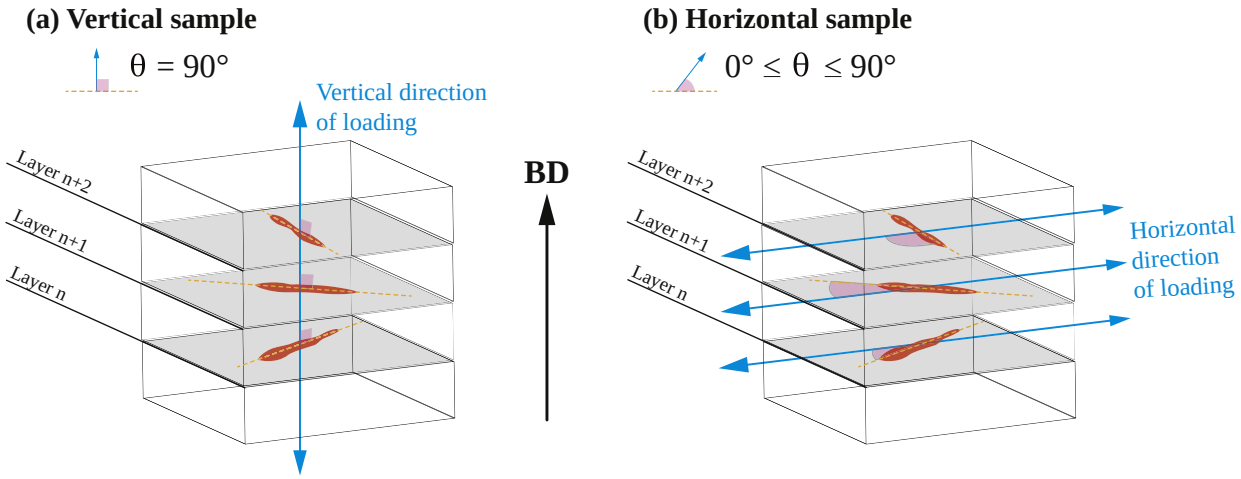


Fig. 16. Variation of angle between preferred lack of fusion pore orientation and direction of loading for (a) vertical and (b) horizontal samples.

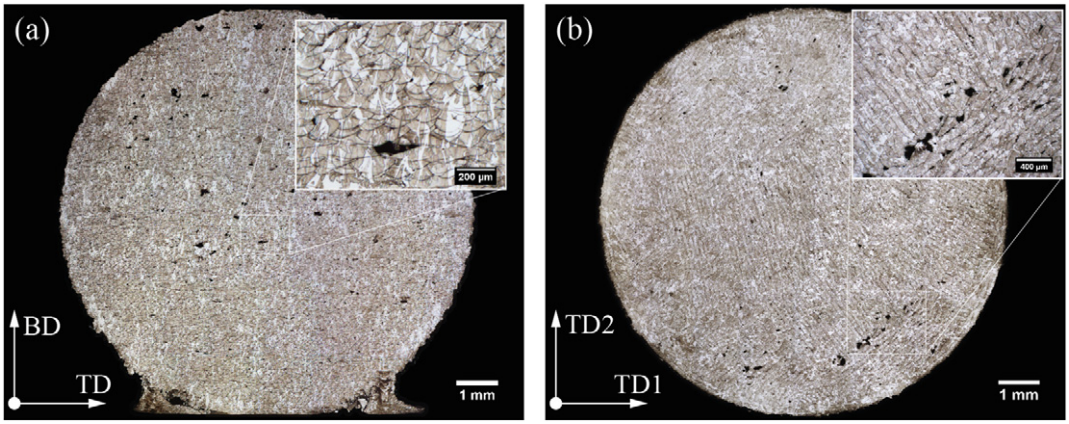


Fig. 17. Etched sections of as-built samples. a) Vertical section of a horizontal sample (HV) with an inset highlighting a pore on the layer boundary. b) Horizontal section of a vertical sample (VH) with an inset showing pores clustered at the edge of a chessboard square from the scanning strategy.

The melt pool boundaries are clearly visible, showing the melt pools are stretched in the loading direction throughout the gauge length. As with the vertical sample, the fracture surface has clearly connected multiple lack of fusion pores. However, the profile between them is not as straight. This is in agreement with the void growth mechanism illustrated in Figs. 15 and 16. The orientation of porosity relative to the direction of loading encourages more ductile failure behaviour.

The positive slopes of the trendlines in Fig. 14 suggest heat treatment induced microstructural changes to improve ductility. Fig. 20 shows heat treated samples (800 °C and 1200 °C) tested to failure and sectioned to revealed the microstructure below the fracture surface. All heat treated samples display more ductile behaviour than their as-built counterparts as the fracture surfaces are less orthogonal to the loading direction. However, the heat treated samples also show evidence that porosity coalescence leading to failure. The microstructural effects on failure behaviour in these samples were consequently of limited significance.

3.7. Implications for quality assurance and heat treatment of structural parts

Results from this study have found porosity dominates failure behaviour in LPBF 316L parts. Material porosity cannot be completely eliminated, but may be managed by optimising process parameters and other process systems such as gas flow and powder feeding to reduce the frequency of large pore formation in the LPBF process. For qualification purposes the Archimedes method is of limited use as it does not describe the size, shape, orientation or distribution of pores. Instead, non-destructive qualification processes such as X-ray microtomography or in-situ process monitoring techniques may be required to qualify parts for critical applications.

As-built LPBF 316L was found to be strong in both horizontal and vertical build orientations, but vertical samples consistently showed low ductility (0.5–3.2%). This is concerning with regard to structural integrity as these samples were also particularly vulnerable to failure

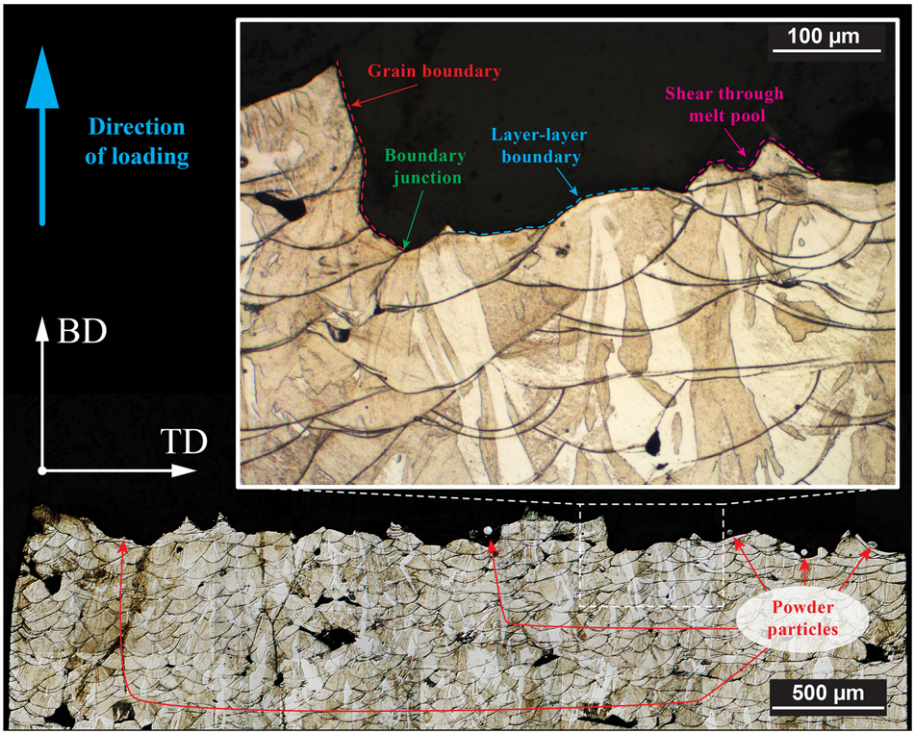


Fig. 18. Composite image of an etched section from a vertical as-built tensile sample tested to failure at 1.46% elongation.

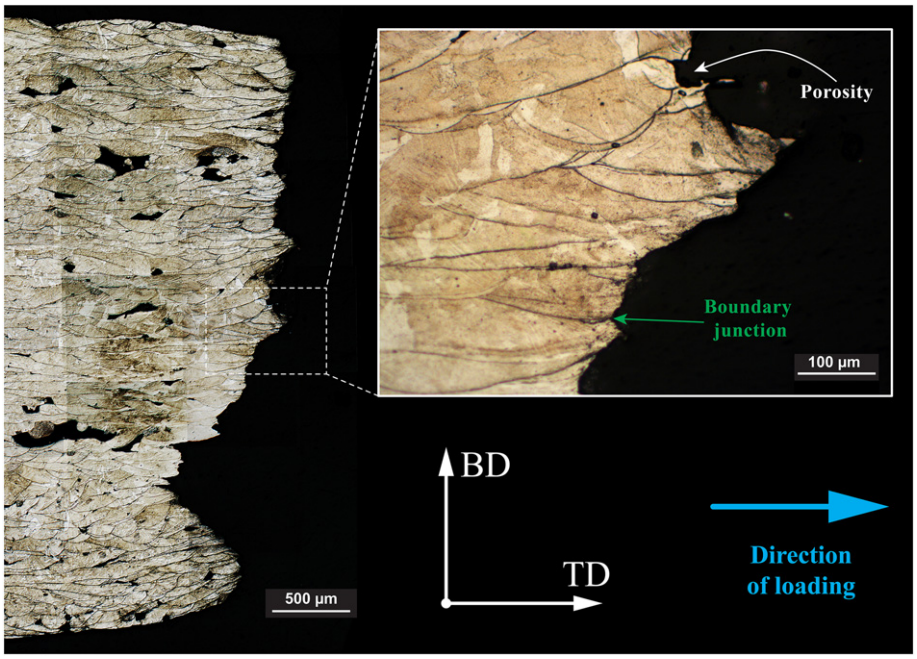


Fig. 19. Composite image of an etched section from a horizontal as-built tensile sample tested to failure at 25.9% elongation.

by crack growth along layer-layer melt pool boundaries to connect pores on the same layer. Heat treatment may decrease this vulnerability. Recovery heat treatments can reduce dislocation density to increase ductility, or homogenisation treatments may reduce the anisotropy of both yield and failure behaviour. However, further research is required to evaluate the effects of heat treatments on other material properties before any recommendation can be made.

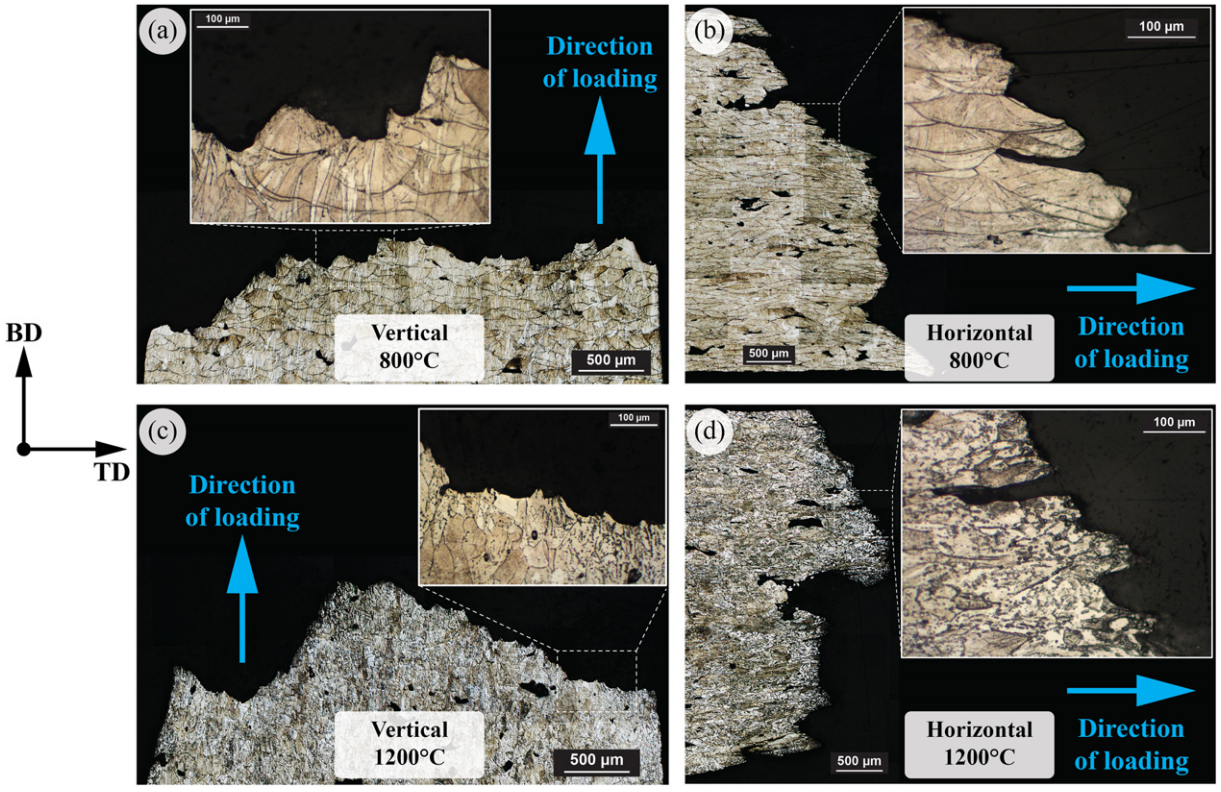


Fig. 20. Etched sections of heat treated samples tensile tested to failure. a) Vertical sample heat treated at 800 °C failing at 10.3% elongation. b) Horizontal sample heat treated at 800 °C failing at 33.8% elongation. c) Vertical sample heat treated at 1200 °C failing at 25.6% elongation. d) Horizontal sample heat treated at 1200 °C failing at 46.9% elongation.

4. Conclusions

In this study heat treatment was used as an investigative tool to isolate the influence of porosity and microstructural features on the mechanical properties of 316L parts produced by LPBF. The investigation led to the following conclusions:

- **Porosity vs yield behaviour:** Porosity does not cause anisotropic yield behaviour. This was demonstrated by heat treatment as isotropic yield behaviour was recovered with increasing heat treatment temperature. Since the pores are unaffected by heat treatment, the cause of yield anisotropy must be microstructural.
- **Porosity vs failure behaviour:** A positive and directionally dependent correlation was found between porosity and ductility. Horizontally built samples, despite higher average levels of porosity, were more ductile than vertically built samples. This was explained by the shape and orientation of pores relative to the loading direction. Most porosity was contained in a few large lack of fusion defects. These high aspect ratio pores had preferential orientation along layer boundaries between adjacent scan tracks. Analysis of fracture subsurface material found failure in both horizontal and vertical loading directions involved coalescence of large pores in the material.
- **Microstructure vs yield behaviour:** Microstructural features were found to greatly influence yield strength of as-built material. Heat treatment, microscopy and tensile testing results were combined to reveal microstructural strengthening mechanisms. In addition to the inherent lattice resistance to dislocation motion, the material was strengthened by grain boundary strengthening, chemical segregation along melt pool boundaries and cell walls, as well as heterogeneous dislocation density within the material. All three strengthening mechanisms may contribute to anisotropic yield behaviour.
- **Microstructure vs failure behaviour:** Failure behaviour was dominated by porosity, but analysis of fracture subsurface material found evidence of microstructural influence as well. As-built vertical samples failed by ductile crack growth along layer-layer melt pool boundaries to connect lack of fusion pores. Coalescence of pores was also found in horizontal samples, but the failure connected pores spread further apart in the direction of loading necessitating more ductile crack growth. Heat treatments dissolving melt pool boundaries increased ductility in both orientations, but anisotropic ductility remains due to the orientation of pores.
- **Heat treatment for practical applications:** Heat treatment was categorised into three regimes; recovery, homogenisation, and annealing. For structural parts, heat treatment may be required to improve ductility. This study found promising results for reducing dislocation density by heat treatment without sacrificing the strengthening contributions of the as-built grain structure and cellular substructure.

This study has shown that whilst relative density is a useful indicator of part quality, it is not alone sufficient to evaluate the structural integrity of LPBF parts. The shape, size, orientation and distribution of pores are crucial parameters affecting mechanical properties. Methods are needed to detect and measure these parameters in order to assure the structural integrity of LPBF parts.

CRediT authorship contribution statement

Tobias Ronneberg: Conceptualization, Formal analysis, Investigation, Methodology, Visualization, Writing - original draft. **Catrin M. Davies:** Conceptualization, Funding acquisition, Project administration, Resources, Supervision, Writing - review & editing. **Paul A. Hooper:** Conceptualization, Funding acquisition, Project administration, Resources, Supervision, Writing - review & editing.

Data availability

The raw data required to reproduce these findings cannot be shared at this time as the data also forms part of an ongoing study.

Declaration of competing interest

None declared.

Acknowledgments

The author thanks AWE plc (contract 30338995) and EPSRC (EP/K503733/1) for their financial support for this research. Thanks are also due to Richard Williams and Henry de Winton for the their assistance and useful discussions.

References

[1] T. Wohlers, Wohlers Report 2018: 3D Printing and Additive Manufacturing State of the Industry: Annual Worldwide Progress Report, Wohlers Associates. 2018.
[2] T.M. Mower, M.J. Long, Mechanical behavior of additive manufactured, powder-bed laser-fused materials, Mater. Sci. Eng. A 651 (2016) 198–213.
[3] W.J. Sames, F. List, S. Pannala, R.R. Dehoff, S.S. Babu, The metallurgy and processing science of metal additive manufacturing, Int. Mater. Rev. 61 (2016) 315–360.
[4] J.J. Lewandowski, M. Seifi, Metal additive manufacturing: a review of mechanical properties, Annu. Rev. Mater. Res. 46 (2016) 151–186.
[5] ASTM International, A276/A276M: Standard Specification for Stainless Steel Bars and Shapes, Standard ASTM International, West Conshohocken, Pennsylvania, 2017.
[6] C. Buchanan, V.-P. Matilainen, A. Salminen, L. Gardner, Structural performance of additive manufactured metallic material and cross-sections, J. Constr. Steel Res. 136 (2017) 35–48.
[7] O. Salman, C. Gammer, A. Chaubey, J. Eckert, S. Scudino, Effect of heat treatment on microstructure and mechanical properties of 316L steel synthesized by selective laser melting, Mater. Sci. Eng. A (2019).
[8] Renishaw, SS 316L-0407 Powder for Additive Manufacturing, Material Data Sheet Renishaw plc, Stone, UK, 2017.
[9] SLM Solutions, Stainless Steel 316L/1.4404/A276, Material Data Sheet SLM Solutions Group AG, Lübeck, Germany, 2019.
[10] Y.-D. Im, K.-H. Kim, K.-H. Jung, Y.-K. Lee, K.-H. Song, Anisotropic mechanical behavior of additive manufactured AISI 316L steel, Metall. Mater. Trans. A (2019) 1–8.
[11] T. Niendorf, S. Leuders, A. Riemer, H.A. Richard, T. Tröster, D. Schwarze, Highly anisotropic steel processed by selective laser melting, Metall. Mater. Trans. B 44 (2013) 794–796.
[12] T. Kurzynowski, K. Gruber, W. Stopyra, B. Kuźnicka, E. Chlebus, Correlation between process parameters, microstructure and properties of 316L stainless steel processed by selective laser melting, Mater. Sci. Eng. A 718 (2018) 64–73.
[13] J. Suryawanshi, K. Prashanth, U. Ramamurty, Mechanical behavior of selective laser melted 316L stainless steel, Mater. Sci. Eng. A 696 (2017) 113–121.
[14] S.A. Khairallah, A.T. Anderson, A. Rubenchik, W.E. King, Laser powder-bed fusion additive manufacturing: physics of complex melt flow and formation mechanisms of pores, spatter, and denudation zones, Acta Mater. 108 (2016) 36–45.
[15] J.-P. Kruth, L. Froyen, J. Van Vaerenbergh, P. Mercelis, M. Rombouts, B. Lauwers, Selective laser melting of iron-based powder, J. Mater. Process. Technol. 149 (2004) 616–622.
[16] N.T. Aboulkhair, N.M. Everitt, I. Ashcroft, C. Tuck, Reducing porosity in AlSi10Mg parts processed by selective laser melting, Addit. Manuf. 1 (2014) 77–86.
[17] Y.M. Wang, T. Voisin, J.T. McKeown, J. Ye, N.P. Calta, Z. Li, Z. Zeng, Y. Zhang, W. Chen, T.T. Roehling, Additively manufactured hierarchical stainless steels with high strength and ductility, Nat. Mater. 17 (2018) 63.
[18] K. Saeidi, X. Gao, Y. Zhong, Z.J. Shen, Hardened austenite steel with columnar sub-grain structure formed by laser melting, Mater. Sci. Eng. A 625 (2015) 221–229.
[19] E. Yasa, J.-P. Kruth, Microstructural investigation of selective laser melting 316L stainless steel parts exposed to laser re-melting, Proc. Eng. 19 (2011) 389–395.
[20] W.E. King, H.D. Barth, V.M. Castillo, G.F. Gallegos, J.W. Gibbs, D.E. Hahn, C. Kamath, A.M. Rubenchik, Observation of keyhole-mode laser melting in laser powder-bed fusion additive manufacturing, J. Mater. Process. Technol. 214 (2014) 2915–2925.

[21] R. Casati, J. Lemke, M. Vedani, Microstructure and fracture behavior of 316L austenitic stainless steel produced by selective laser melting, J. Mater. Sci. Technol. 32 (2016) 738–744.
[22] B. Zhang, Y. Li, Q. Bai, Defect formation mechanisms in selective laser melting: a review, Chin. J. Mech. Eng. 30 (2017) 515–527.
[23] S. Gorsse, C. Hutchinson, M. Gouné, R. Banerjee, Additive manufacturing of metals: a brief review of the characteristic microstructures and properties of steels, Ti-6Al-4V and high-entropy alloys, Sci. Technol. Adv. Mater. 18 (2017) 584–610.
[24] D. Wang, C. Song, Y. Yang, Y. Bai, Investigation of crystal growth mechanism during selective laser melting and mechanical property characterization of 316L stainless steel parts, Mater. Des. 100 (2016) 291–299.
[25] K. Prashanth, J. Eckert, Formation of metastable cellular microstructures in selective laser melted alloys, J. Alloys Compd. 707 (2017) 27–34.
[26] Y. Zhong, L. Liu, S. Wikman, D. Cui, Z. Shen, Intragranular cellular segregation network structure strengthening 316L stainless steel prepared by selective laser melting, J. Nucl. Mater. 470 (2016) 170–178.
[27] M.-S. Pham, B. Dovgyy, P.A. Hooper, Twinning induced plasticity in austenitic stainless steel 316L made by additive manufacturing, Mater. Sci. Eng. A 704 (2017) 102–111.
[28] W. Shifeng, L. Shuai, W. Qingsong, C. Yan, Z. Sheng, S. Yusheng, Effect of molten pool boundaries on the mechanical properties of selective laser melting parts, J. Mater. Process. Technol. 214 (2014) 2660–2667.
[29] B. Weiss, R. Stickler, Phase instabilities during high temperature exposure of 316 austenitic stainless steel, Metall. Mater. Trans. B 3 (1972) 851–866.
[30] J.C. Lippold, D.J. Kotecki, Welding Metallurgy and Weldability of Stainless Steels, Wiley, Hoboken, New Jersey, 2005. https://doi.org/10.1002/9781118960332.
[31] R. Cunningham, S.P. Narra, C. Montgomery, J. Beuth, A. Rollett, Synchrotron-based X-ray microtomography characterization of the effect of processing variables on porosity formation in laser power-bed additive manufacturing of Ti-6Al-4V, Jom 69 (2017) 479–484.
[32] M. Seifi, A. Salem, J. Beuth, O. Harrysson, J.J. Lewandowski, Overview of materials qualification needs for metal additive manufacturing, JOM 68 (2016) 747–764.
[33] C. Kamath, B. El-dasher, G.F. Gallegos, W.E. King, A. Sisto, Density of additively-manufactured, 316L SS parts using laser powder-bed fusion at powers up to 400 W, Int. J. Adv. Manuf. Technol. 74 (2014) 65–78.
[34] Z. Sun, X. Tan, S.B. Tor, W.Y. Yeong, Selective laser melting of stainless steel 316L with low porosity and high build rates, Mater. Des. 104 (2016) 197–204.
[35] A. AlFaify, J. Hughes, K. Ridgway, Controlling the porosity of 316L stainless steel parts manufactured via the powder bed fusion process, Rapid Prototyp. J. 25 (2019) 162–175.
[36] LPW Technology, Testing Powder for Optimal Processing Window, Case Study LPW Technology LTD., Cheshire, UK, 2017.
[37] A.B. Spierings, M. Schneider, R. Eggenberger, Comparison of density measurement techniques for additive manufactured metallic parts, Rapid Prototyp. J. 17 (2011) 380–386.
[38] A. Wilson-Heid, T. Novak, A.M. Beese, Characterization of the effects of internal pores on tensile properties of additively manufactured austenitic stainless steel 316L, Exp. Mech. 59 (2019) 793–804.
[39] C. Qiu, M. Al Kindi, A.S. Aladawi, I. Al Hatmi, A comprehensive study on microstructure and tensile behaviour of a selectively laser melted stainless steel, Sci. Rep. 8 (2018) 7785.
[40] Nabertherm GmbH, Thermal Process Technology, Product Catalogue Nabertherm GmbH, Lilienthal, Germany, 2016.
[41] ASTM International, E407: Standard Practice for Microetching Metals and Alloys, Standard ASTM International, West Conshohocken, Pennsylvania, 2015.
[42] T. Ferreira, W. Rasband, ImageJ User Guide, ImageJ/Fiji IJ 1.46r (2012) 132–135.
[43] ASTM International, E8/E8M: Standard Test Methods for Tension Testing of Metallic Materials, Standard ASTM International, West Conshohocken, Pennsylvania, 2013.
[44] GOM GmbH, GOM Correlate, Precise Industrial 3D Metrology GOM GmbH, Braunschweig, Germany, 2018.
[45] K. Darvish, Z. Chen, T. Pasang, Reducing lack of fusion during selective laser melting of CoCrMo alloy: effect of laser power on geometrical features of tracks, Mater. Des. 112 (2016) 357–366.
[46] M. Tang, P.C. Pistorius, J.L. Beuth, Prediction of lack-of-fusion porosity for powder bed fusion, Addit. Manuf. 14 (2017) 39–48.
[47] T. Mukherjee, J. Zuback, A. De, T. DebRoy, Printability of alloys for additive manufacturing, Sci. Rep. 6 (2016) 19717.
[48] Renishaw, Renishaw Additive Manufacturing System AM250, User Guide Renishaw plc, Stone, United Kingdom, 2014.
[49] S. Mahajan, C. Pande, M. Imam, B. Rath, Formation of annealing twins in fcc crystals, Acta Mater. 45 (1997) 2633–2638.
[50] L. Clarebrough, M. Hargreaves, G. West, The release of energy during annealing of deformed metals, Proc. R. Soc. Lond. A Math. Phys. Sci. 232 (1955) 252–270.
[51] C. Blochwitz, W. Tirschler, Influence of texture on twin boundary cracks in fatigued austenitic stainless steel, Mater. Sci. Eng. A 339 (2003) 318–327.
[52] F. Yan, W. Xiong, E. Faierson, G.B. Olson, Characterization of nano-scale oxides in austenitic stainless steel processed by powder bed fusion, Scr. Mater. 155 (2018) 104–108.